



This is a repository copy of *Impact of Ni²⁺ on the structural, optical, electrical, and dielectric properties of Cu_{0.25}Co_{0.25}Mg_{0.5-x}Ni_xCe_{0.03}Fe_{1.97}O₄ spinel ferrites synthesized via sol-gel auto combustion (SGAC) route.*

White Rose Research Online URL for this paper:

<https://eprints.whiterose.ac.uk/197491/>

Version: Accepted Version

Article:

Ur Rehman, A., Abbas, G., Ayoub, B. et al. (9 more authors) (2023) Impact of Ni²⁺ on the structural, optical, electrical, and dielectric properties of Cu_{0.25}Co_{0.25}Mg_{0.5-x}Ni_xCe_{0.03}Fe_{1.97}O₄ spinel ferrites synthesized via sol-gel auto combustion (SGAC) route. *Materials Science and Engineering: B*, 291. 116407. ISSN 0921-5107

<https://doi.org/10.1016/j.mseb.2023.116407>

Article available under the terms of the CC-BY-NC-ND licence (<https://creativecommons.org/licenses/by-nc-nd/4.0/>).

Reuse

This article is distributed under the terms of the Creative Commons Attribution-NonCommercial-NoDerivs (CC BY-NC-ND) licence. This licence only allows you to download this work and share it with others as long as you credit the authors, but you can't change the article in any way or use it commercially. More information and the full terms of the licence here: <https://creativecommons.org/licenses/>

Takedown

If you consider content in White Rose Research Online to be in breach of UK law, please notify us by emailing eprints@whiterose.ac.uk including the URL of the record and the reason for the withdrawal request.



eprints@whiterose.ac.uk
<https://eprints.whiterose.ac.uk/>

Impact of Ni²⁺ on the structural, optical, electrical, and dielectric properties of Cu_{0.25}Co_{0.25}Mg_{0.5-x}Ni_xCe_{0.03}Fe_{1.97}O₄ spinel ferrites synthesized via Sol-gel auto combustion (SGAC) route

Atta Ur Rehman^a, Ghulam Abbas^{b,c}, Bilal Ayoub^b, Nasir Amin^a, M. Afzaal^b, A. Ghuffar^b, Nicola A Morley^c, Maria Akhtar^a, Muhammad Imran Arshad^{*a}, Muhammad Arshad^{f**}

^aDepartment of Physics, Government College University, Faisalabad, Pakistan.

^bDepartment of Physics, Riphah International University, Faisalabad Campus, Pakistan.

^cDepartment of Physics, Ghazi University, Dera Ghazi Khan.

^eDepartment of Materials Science and Engineering, The University of Sheffield, UK, S1 3JD

^fNanoscience's & Technology Department, National Centre for Physics (NCP), Quaid-i-Azam University (QAU) Campus, Islamabad Pakistan.

Corresponding Author: *miarshadgcuf@gmail.com, ** arshad_pr2002@yahoo.com

Abstract

The sol-gel auto-combustion (SGAC) route was used to prepare the Cu_{0.25}Co_{0.25}Mg_{0.5-x}Ni_xCe_{0.03}Fe_{1.97}O₄ [Ni-CCMCF] (0.0 ≤ x ≤ 0.5 with the step interval of 0.125) spinel ferrites (SFs). The formation of a single-phase spinel matrix was observed by X-ray diffraction (XRD) analysis. Moreover, the sharp peaks of XRD spectra confirmed the high crystallinity of the as-prepared spinel ferrites. The crystallite size (*D*) was reduced from (57.33–10.51) ± 0.05 nm and for the pure CCMCF sample, the specific surface area was 20.36 m²/g. The variation absorption bands at tetrahedral and octahedral sites along five Raman modes in Raman spectra were also confirmed in the spinel matrix of the Ni-CCMCF samples. The optical bandgap increased from 0.87 eV to 1.68 eV was observed with the replacement of dopant ions. Furthermore, the minimum resistivity was observed both in Ferro and para regions for the pure CCMCF sample. The tangent loss and dielectric constant were reduced, but *ac* conductivity was enhanced with increasing frequency and all the dielectric parameters have a minimum value for pure the CCMCF sample. X-ray photoelectron spectroscopy (XPS) and Energy Dispersive X-ray Spectroscopy (EDS) confirmed the successful incorporation of Ni²⁺ in the CCMCF sample. Therefore, due to the low tangent loss, the pure CCMCF sample will be used for high resonant frequency applications.

Keywords: sol-gel auto-combustion; crystallinity; crystallite size; specific surface area; high resonant frequency.

1 Introduction

Spinel ferrites (SFs) are iron oxides with the general formula AB_2O_4 , where A is a divalent cation, such as Co^{2+} , Cu^{2+} , Ni^{2+} , Mg^{2+} , Zn^{2+} , or Cd^{2+} , and B is a trivalent cation including Fe^{3+} , Al^{3+} , La^{3+} , Ce^{3+} , Ho^{3+} , or Eu^{3+} , etc. [1]. Because of their wide variety of applications in high-density magnetic recording [2], medicine [3], sensors [4], magnetic fluids [5], and other fields, ferrites are gaining more significance. Various methods were used for spinel ferrites preparation including the glass crystallization method [6], sol-gel auto combustion (SGAC) route [7-9], co-precipitation process [10-14], and solid-state reaction route [15]. The modified Pechini's method of synthesis of $NiFe_2O_4$ (NFO) spinel ferrite was reported by Dominguez-Arvizu *et al.*, [16]. The scattering and absorption coefficient was observed using optical analysis and reported the optical bandgap is 1.6 eV for as-prepared Ni-ferrite. The specific surface area was $50\text{ m}^2/\text{g}$ and the crystallite size was 25 nm. Peng *et al.*, [17] studied a hydrothermal and calcination technique used to prepare NFO magnetic material. The average crystallite size was 17.8 nm and a specific surface area of $76.2\text{ m}^2/\text{g}$. The optical bandgap for NFO was 1.52 eV [18] and for $CoFe_2O_4$ (CFO) was 1.3 eV [18]. Gaikwad *et al.*, [19] studied the electrostatic synthesis of CFO films and their application in long-term hydrogen generation. The optical band gap reported was 2.57 eV for the CFO sample. Kumar *et al.*, [20] reported a series of $Ni_xMg_{1-x}Fe_2O_4$ ferrites where $x = 0.0, 0.25, 0.5, 0.75, \text{ and } 1$ synthesized *via* the nitrate-citrate method. Moreover, they observed that the lattice constant was reduced due to the replacement of greater ionic radii Mg^{2+} (0.72 \AA) ion smaller ionic radii Ni^{2+} (0.69 \AA) ion. The maximum tangent loss was observed for the Ni^{2+} doping $x = 0.25$. Yu *et al.*, [21] reported $Ni_{0.2}Mg_{0.1}Co_{0.7}Fe_2O_4$ ferrite prepared using the SGAC technique. The observed crystallite size was 60.89 nm and the optical bandgap was 2.26 eV. $Ni_{0.2}Cu_{0.2}Co_{0.6}Fe_2O_4$ ferrite reported by Pan *et al.*, [22] prepared *via* SGAC route. They observed a lattice constant of 8.3665 \AA and the crystallite size was 60.45 nm. $Ni_{0.5}Mg_{0.5}Fe_2O_4$ sample was prepared *via* the chemical co-precipitation method and studied the frequency dependence of dielectric dispersion and successfully explained using the hopping mechanism. Because the sample has a lower dielectric loss, and is suitable for microwave applications [23]. Ali *et al.*, [24] reported that the crystallite size is small enough to achieve a significant signal-to-noise ratio in the recording medium. The optimized dielectric and magnetic parameters suggest that the material $Mg_{0.6}Ni_{0.4}Co_{0.4}Fe_{1.6}O_4$ could be used in recording media and microwave devices. We have prepared $Cu_{0.25}Co_{0.25}Mg_{0.5-x}Ni_xCe_{0.03}Fe_{1.97}O_4$ ($0.0 \leq x \leq 0.5$ with the step interval of 0.125) SFs

via the SGAC method and investigated their structural, optical, electrical, dielectric, and magnetic properties.

2. Materials and methods

2.1 Materials and method of preparation used

To prepare $Cu_{0.25}Co_{0.25}Mg_{0.5-x}Ni_xCe_{0.03}Fe_{1.97}O_4$ [Ni-CCMCF] ferrite samples the SGAC method was used. The chemicals $Ce(NO_3)_3 \cdot 6H_2O$, $Ni(NO_3)_2 \cdot 6H_2O$, $Co(NO_3)_2 \cdot 6H_2O$, $Mg(NO_3)_2 \cdot 6H_2O$, $Fe(NO_3)_3 \cdot 9H_2O$, and $Cu(NO_3)_2 \cdot 3H_2O$ was taken for Ni-CCMCF sample preparation. A stoichiometric amount of these materials was taken and dissolved in distilled water. The citric acid in 1:1 with metal nitrates was added to the chemicals with continuous stirring. It acts as a chelating agent for metal ions and added ammonia dropwise to maintain its pH to 7. The heat was maintained at 80 °C unless the gel was formed and then turned to 300 °C that caused the ash formation. Sintering was performed at 800 °C for 8h. The obtained material was grounded and used for different characterizations. The Ni-CCMCF sample preparation steps are depicted in Fig.1.

2.2 Characterizations used

X-ray diffraction (XRD) in the range of 20° – 60° was used for the identification of crystal structure and other structural parameters-related information. To study the absorption bands, Fourier transforms infrared (FTIR) spectroscopy was utilized. The information concerning vibrational modes was collected using Raman spectroscopy. The energy bandgap (E_g) was calculated by using UV–visible spectroscopy. Keithley Electrometer Model 2401 was used to find out the temperature-dependent resistivity in the temperature range of 323 – 673 K. Dielectric parameters were measured using IM3533, LCR Meter. Morphology and elemental analysis have been performed using Field Effect Scanning Electron Microscope (FE-SEM) and Energy Dispersive X-ray Spectroscopy (EDS) sigma 500 VP, ZEISS, Germany.

X-ray photoelectron spectroscopy (XPS) measurements are performed using a Scienta-Omicron XPS instrument equipped with a micro-focused monochromatic Al K-Alpha X-ray source. The x-ray source was operated at 15 KeV (400-micron spot size), analyzer energy (CAE) 100 eV for survey scan, and 20 eV for specified scans. The data acquisition was accomplished with Matrix software and data analysis was performed with Igor pro along with XPS fit procedures. The curve fitting of XPS data is performed by Gaussian-Lorentzian line shape after performing the Shirley background corrections. Adventurous C1s core at 284.8 eV used for calibration of binding energy levels.

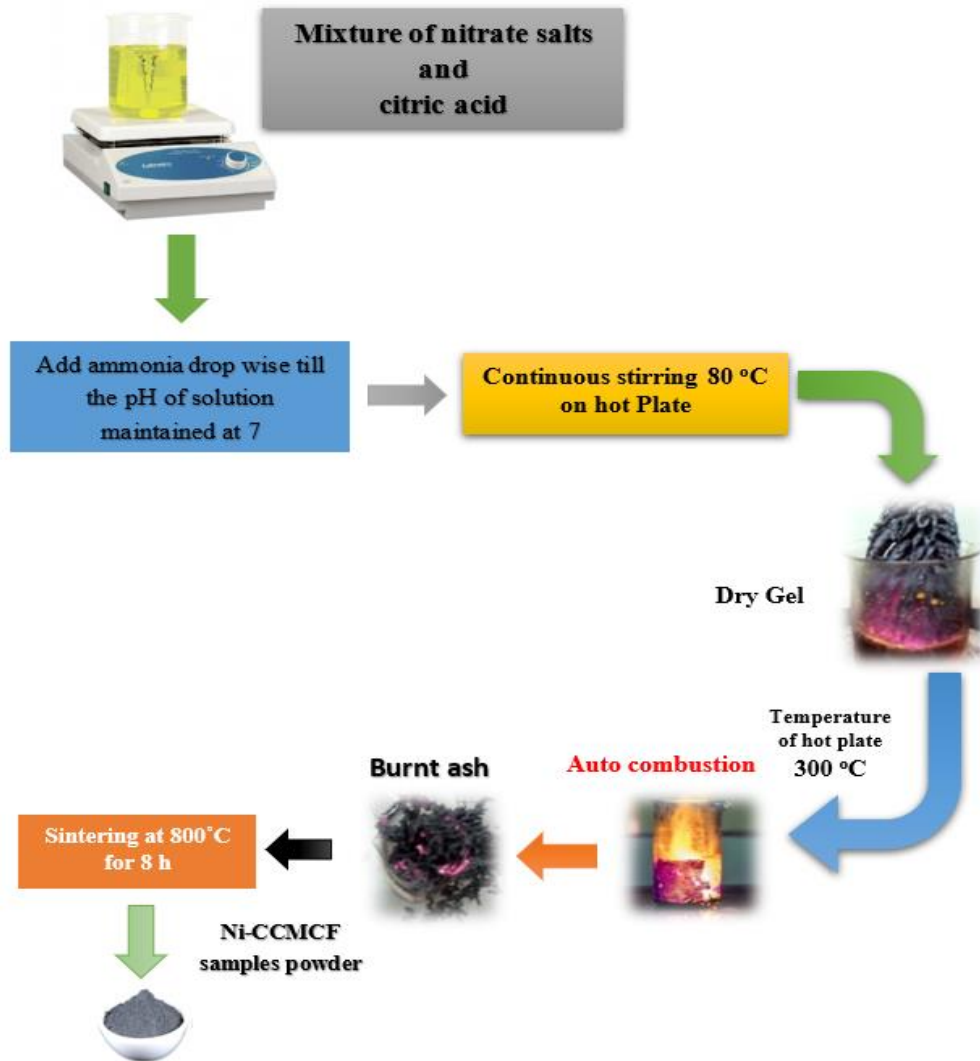


Fig. 1 Ni-CCMCF samples preparation steps

3. Results and discussion

3.1 Phase and structural parameters analysis of Ni-CCMCF samples

The XRD patterns of as-synthesized samples at different Ni²⁺ concentrations are well-matched with the single-phase cubic spinel matrix ferrite (JCPDS # 74-2081) with diffraction peaks at different 2θ values labeled with (220), (311), (222), (400), (422) and (511) depicted in Fig.2. The sharp peaks of the XRD pattern (Fig.2) revealed the high crystallinity of the as-prepared samples.

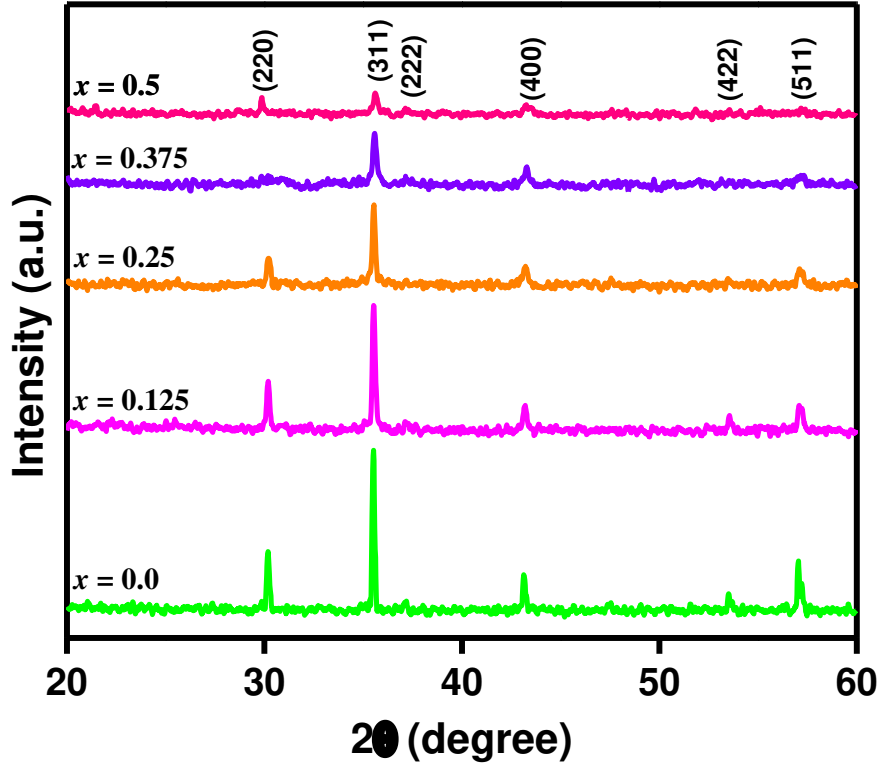


Fig. 2 XRD pattern for Ni-CCMCF samples

The full width at half maxima (β) was estimated by fitting the diffraction peaks and reported in Table 1. The values of “ β ” were raised with the accumulation of Ni^{2+} at the respective lattice site in the spinel matrix. Using the value of “ β ”, the crystallite size (D) was determined by employing the equation (1) [25]:

$$D = \frac{n\lambda}{\beta \cos\theta} \quad (1)$$

The crystallite size reduced from 57.33 nm to 10.51 nm with the replacement of dopant ions (Fig.3(a)). The distance between planes or layers of the atom in the crystal structure is known as d-spacing or interplanar spacing (d). Therefore, the values of “ d ” were estimated using the relation (2) [25]:

$$d = \frac{n\lambda}{2\sin\theta} \quad (2)$$

The d-spacing of as-prepared samples also reduced as the Ni^{2+} doping increased. The d-spacing used to calculate the lattice constant (a) of the Ni-CCMCF samples by employing the following equation [25]:

$$a = d\sqrt{h^2 + k^2 + l^2} \quad (3)$$

The lattice constant was reduced from 8.3694 Å to 8.3410 Å for $x = 0.0 - 0.5$. The trend of d-spacing and lattice constant is depicted in Fig.3(b). The unit cell volume (V) was determined using equation (4) [26, 27]:

$$V = a^3 \quad (4)$$

The value of “ V ” was decreased from 586.25 Å³ to 580.31 Å³. The hopping length for tetrahedral (A) and octahedral (B) sites, “ L_A ” and “ L_B ”, respectively. Both “ L_A ” and “ L_B ” depend on the lattice constant and are calculated using the given relation (5) and (6) [27, 28]:

$$L_A = \frac{a\sqrt{3}}{4} \quad (5)$$

$$L_B = \frac{a\sqrt{2}}{4} \quad (6)$$

The hopping at A - and B - sites have a similar trend as the lattice constant. The values of “ L_A ” and “ L_B ” were reduced with the addition of Ni²⁺ ions in the lattice site and are tabulated in Table 1. The charge carriers in ferrites are not free but are firmly concentrated in the d-shell, which might be attributed to the creation of polarons. When an electronic carrier is trapped at specific sites due to the displacement of nearby atoms or ions, a minor polaron defect is produced [1, 11]. For all of the samples analyzed by the relation (7) [11], an attempt was made to calculate the polaron radius (γ).

$$\gamma = \frac{1}{2} \sqrt[3]{\frac{\pi a^3}{576}} \quad (7)$$

The calculated values of the polaron radius are given in Table 1. The fact that hopping length and polaron radius decreased as Ni²⁺ concentration (x) increased shows that charge carriers need less energy to jump from one lattice site to the other. The hopping length at both lattice sites and polaron radius is depicted in Fig.3(c). The X-ray density (d_x) depends on the molecular mass (M) and lattice constant (a) as shown in equation (8) [29] and calculated values of X-ray density are given in Table 1. The X-ray density increased as the Ni²⁺ ions concentration.

$$d_x = \frac{8M}{N_A a^3} \quad (8)$$

The specific surface area (S) revealed by ferrite is highly dependent on the technique of preparation. Due to smaller crystallite sizes having a larger specific surface area, they have better photocatalytic activity because of a greater number of active sites. The specific surface area was estimated using the relation (9) [30] and is given in Table 1.

$$S = \frac{6000}{\rho_x \times D} \quad (9)$$

The specific surface area was 20.36 m²/g, 23.82 m²/g, 25.00 m²/g, 33.15 m²/g, and 102.154 m²/g for $x = 0.0 - 0.5$ (with the step interval of 0.125). The observed specific surface area of Ni-CCMCF samples was increased with the substitution of Ni²⁺ at their respective lattice sites. The increase in specific surface area may be due to the reduction of crystallite size. The lattice parameters including the packing factor (p) [30], strain (ε) [30], and dislocation density (δ) [30] were determined by using formulas from equations (10), (11), and (12) and given in Table 1.

$$p = \frac{D}{d} \quad (10)$$

$$\varepsilon = \frac{1}{d^2} \quad (11) \quad \delta = \frac{1}{D^2} \quad (12)$$

It can be observed from Table 1 that the strain and dislocation density have a maximum value for the Ni²⁺ concentration $x = 0.5$ and the packing factor was minimum for the $x = 0.5$. The dislocation line density is graphically depicted in Fig.3(a). As the concentrations of Ni²⁺ in the sample increased, the packing factor of as-prepared ferrites was reduced, as shown in Table 1. It might be because smaller crystallites should be packed more tightly, leaving fewer pores between them. This would increase sample density and reduce the packing factor. The Ni²⁺ incorporated into a CCMCF ferrite matrix increases lattice strain. The increasing strain in the present case is caused by lattice shrinkage. The calculation results in Table 1 revealed that the dislocation line density exhibits a trend toward increase. A decrease in the sample's crystallinity is indicated by a rise in the dislocation line density. This can be a result of the low sintering temperature used to prepare the sample. To improve the crystallinity of samples, the sintering temperature or sintering duration should be appropriately increased [31].

Table 1 Lattice parameters of the as-prepared samples

Parameters	$x = 0.0$	$x = 0.125$	$x = 0.25$	$x = 0.375$	$x = 0.5$
β (degree) ± 0.05	0.1518	0.1812	0.1940	0.2627	0.8281
D (nm) ± 0.05	57.33	48.02	44.87	33.14	10.51
d (Å)	2.5234	2.5221	2.5213	2.5188	2.5149
a (Å)	8.3694	8.3647	8.3622	8.3542	8.3410
V (Å) ³	586.25	585.27	584.75	583.06	580.31
L_A (Å)	3.6239	3.6219	3.6208	3.6173	3.6116
L_B (Å)	2.9585	2.9569	2.9560	2.9532	2.9485
γ (Å)	0.7495	0.7491	0.7488	0.7481	0.7469
d_x (g/cm ³)	5.1385	5.2448	5.3471	5.4606	5.5848
S (m ² /g)	20.36	23.82	25.00	33.15	102.15
p	227.19	190.42	177.98	131.57	41.81
ε	0.0020	0.0024	0.0026	0.0036	0.0112
$\delta \times 10^{-4}$ (nm ⁻²) ± 0.05	3.04	4.33	4.96	9.10	90.40

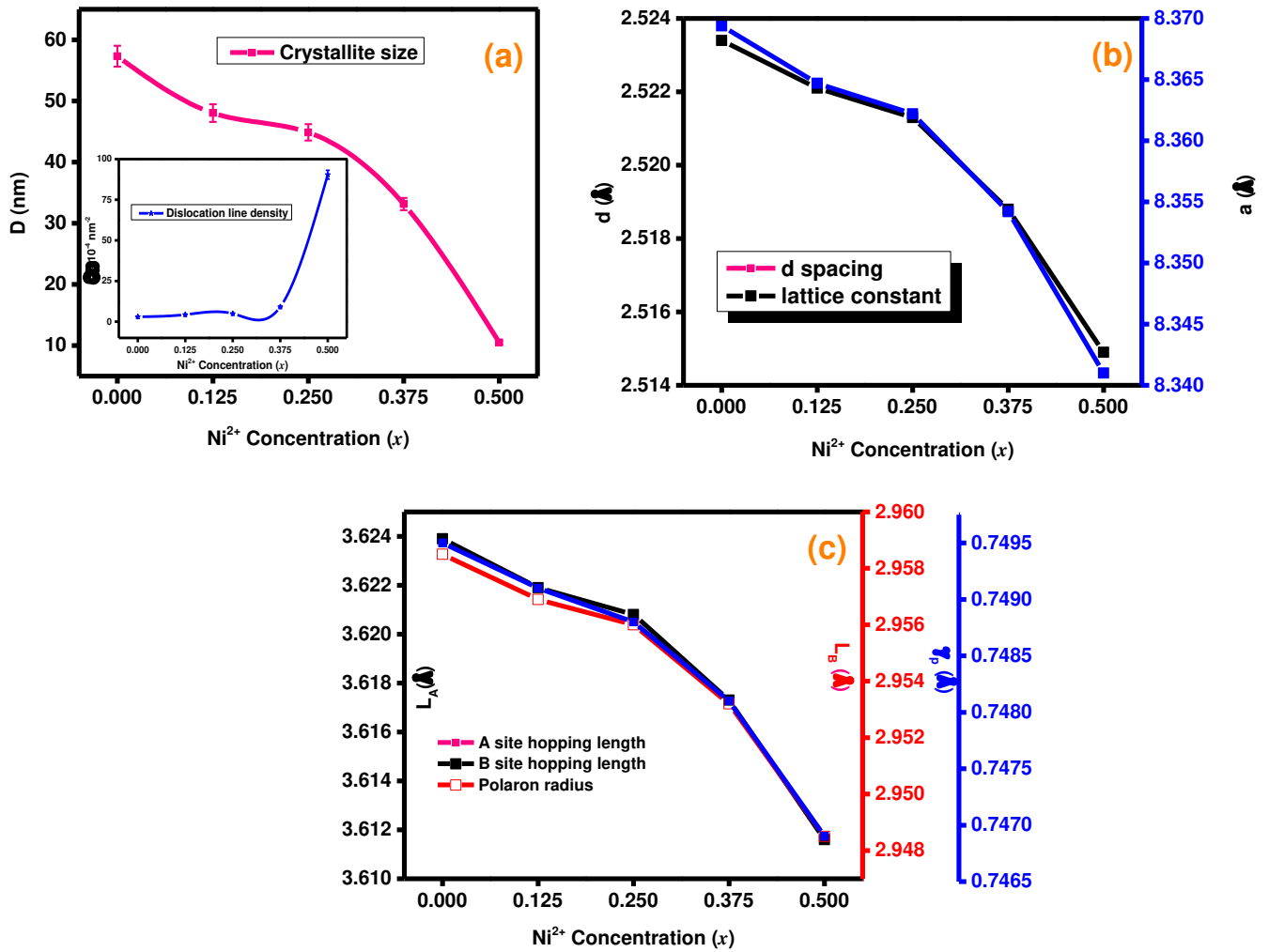


Fig. 3 Ni²⁺ concentration (x) versus (a) crystallite size and dislocation line density (b) d-spacing and lattice constant (c) A and B sites hopping length along polaron radius

3.2 Absorption bands analysis of Ni-CCMCF samples

Fig. 4 depicted FTIR spectra in the range of 400 – 4000 cm⁻¹ for Ni-CCMCF samples. The high-frequency bands (ν_1) in the range of (556.52 – 588.01) cm⁻¹ and the low-frequency bands (ν_2) in the range of (408 – 433.36) cm⁻¹ corresponded to tetrahedral and octahedral sites metal-oxygen stretching vibrations, respectively [32]. The values of low and high-frequency bands are tabulated in Table 2. The difference in the high and low-frequency bands also confirmed the replacement of Ni²⁺ at their respective lattice site. The peaks around 1120.87 cm⁻¹ are due to the C-O bond and the band at 1396 cm⁻¹ was due to N-O stretching vibration [33]. The peaks that appeared around 1559.03 – 1565.51 cm⁻¹ are due to atmospheric CO₂ [34]. The force constants were determined using relation (13) [35] and values are tabulated in Table 2.

$$K = 4\pi^2 c^2 \nu^2 \mu \quad (13)$$

where μ is known as reduced mass (2.601×10^{-23} g). The force constant at the tetrahedral site (K_1) lies in the range of $(2.86 - 3.19) \times 10^5$ dynes/cm⁻¹ and at the octahedral site (K_2) lies in the range of $(1.54 - 1.73) \times 10^5$ dynes/cm⁻¹ (graphically depicted in Fig. 5).

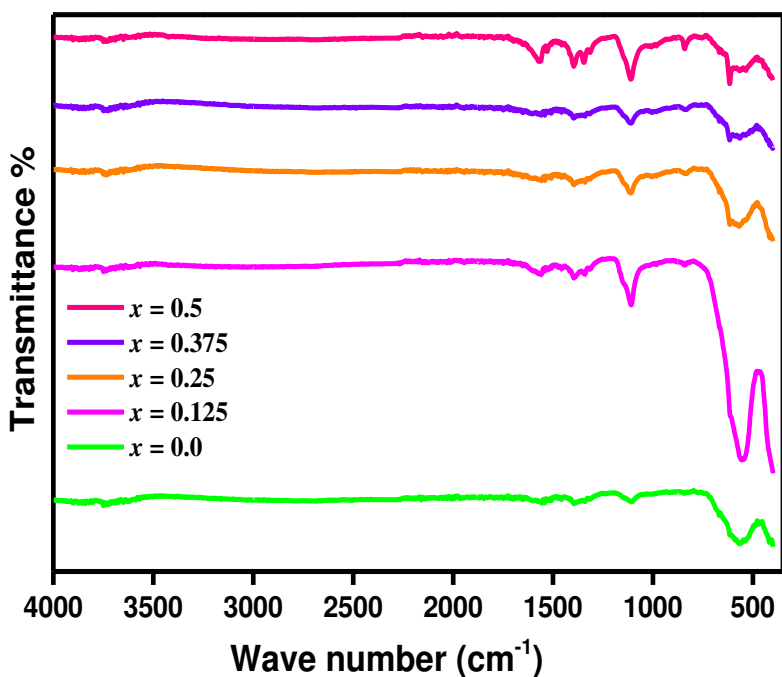


Fig. 4 Absorption bands spectra for Ni-CCMCF samples

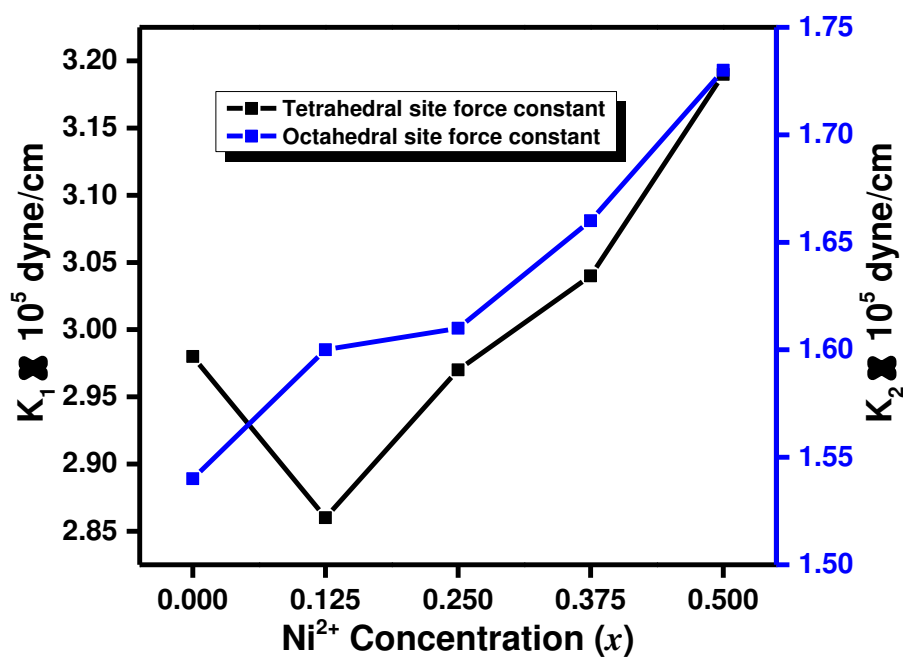


Fig. 5 Ni²⁺ concentration (x) versus tetra and octahedral site force constants

Table 2 FTIR parameters of the as-synthesized samples

x	ν_1	ν_2	K_1	K_2
	(cm ⁻¹)		$\times 10^5$ (dyne/cm)	
0.0	568.52	408.63	2.98	1.54
0.125	556.52	417.12	2.86	1.60
0.25	567.32	418.07	2.97	1.61
0.375	574.13	425.08	3.04	1.66
0.5	588.01	433.36	3.19	1.73

3.3 Raman modes analysis of Ni-CCMCF samples

Raman spectroscopy was utilized to gain information about lattice structure and vibrational modes associated with spinel ferrites [11]. The Raman spectra were recorded in the frequency range of 200 – 800 cm⁻¹ are depicted in Fig. 6. The variation in five Raman modes E_g , T_{2g} , T_{2g} (2), A_{1g} (1), A_{1g} (2) confirmed the substitution of Ni²⁺ ion spinel structure at their respective sites in Ni-CCMCF samples. Table 3 makes it obvious that all as-prepared samples Raman modes change when the Ni²⁺ content increases. This change in Raman modes is the result of the inclusion of Ni²⁺ ions in spinel ferrite samples, which redistributes cations between octahedral and tetrahedral sites. Additionally, phonon confinement and differences in phonon relaxation with the smaller particle size can be responsible for the wide shift of the Raman modes in the samples. It is clear from Fig. 6 that the as-prepared samples have a monophasic composition, which supports the findings of the XRD investigation and excludes the presence of any other peaks that correspond to any other iron oxide phases. The values of observed vibrational modes are listed in Table 3. The Raman mode “ E_g ” lies in the range 320 cm⁻¹ – 327 cm⁻¹, the vibrational mode “ T_{2g} (1)” lies in the range 462 cm⁻¹ – 466 cm⁻¹, and the mode “ T_{2g} (2)” has a range 532 cm⁻¹ – 590 cm⁻¹ belongs to Raman modes at the octahedral site. The Raman band “ A_{1g} (2)” having a range of 685 cm⁻¹ to 690 cm⁻¹ corresponds to the tetrahedral Raman mode in the spinel matrix. The shoulder peaks observed correspond to “ A_{1g} (1)” which lies in the range of 613 cm⁻¹ to 617 cm⁻¹.

Table 3 Raman modes for Ni-CCMCF samples

x	E_g	T_{2g} (2)	T_{2g} (2)	A_{1g} (1)	A_{1g} (2)
	cm ⁻¹				
0.0	327	462	590	616	687
0.125	320	464	553	613	685
0.25	327	464	532	613	688
0.375	327	466	551	617	690
0.5	327	462	543	614	685

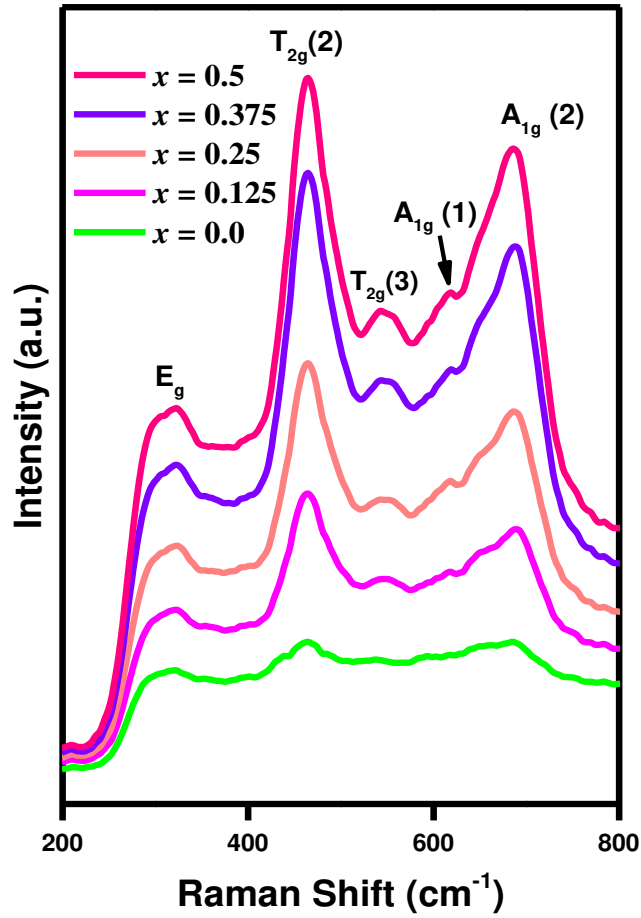


Fig. 6 Raman spectra for as-prepared samples

3.4 Energy bandgap analysis of Ni-CCMCF samples

When discussing optical materials, the optical absorption and energy band gap of a material are the most significant characteristics. Tauc's equation (14) [30, 36] was utilized to estimate the energy bandgap of Ni-CCMCF samples.

$$ahv = B(hv - E_g)^m \quad (14)$$

where, “ m ” is constant which may be 2 or $\frac{1}{2}$, hv = photon energy, and B = transition probability dependence constant. The absorption coefficient (α) was determined *via* equation (15) [30]:

$$\alpha = 2.303 \frac{\log(A)}{l} \quad (15)$$

where “ A ” is absorbance and “ l ” is the path length of light in which absorbance takes place. In the present study, the energy bandgap (E_g) was evaluated by extrapolating the linear portion of plot incident photon energy (hv) *versus* $(ahv)^2$ for Ni-CCMCF samples. This is known as Tauc's plots and for as-prepared samples depicted in Fig.7. The energy bandgap (E_g) decreased with increasing Ni^{2+} content. The energy band gap was reduced from 1.33 eV – 2.26 eV for Ni^{2+} concentration $x = 0.0 - 0.5$. Numerous structural parameters, including crystallite size,

lattice parameters, etc., have an impact on the bandgap energy [37]. Some of them are highlighted: the bandgap energy was increased with decreasing lattice constant and crystallite size (as shown in Table 1).

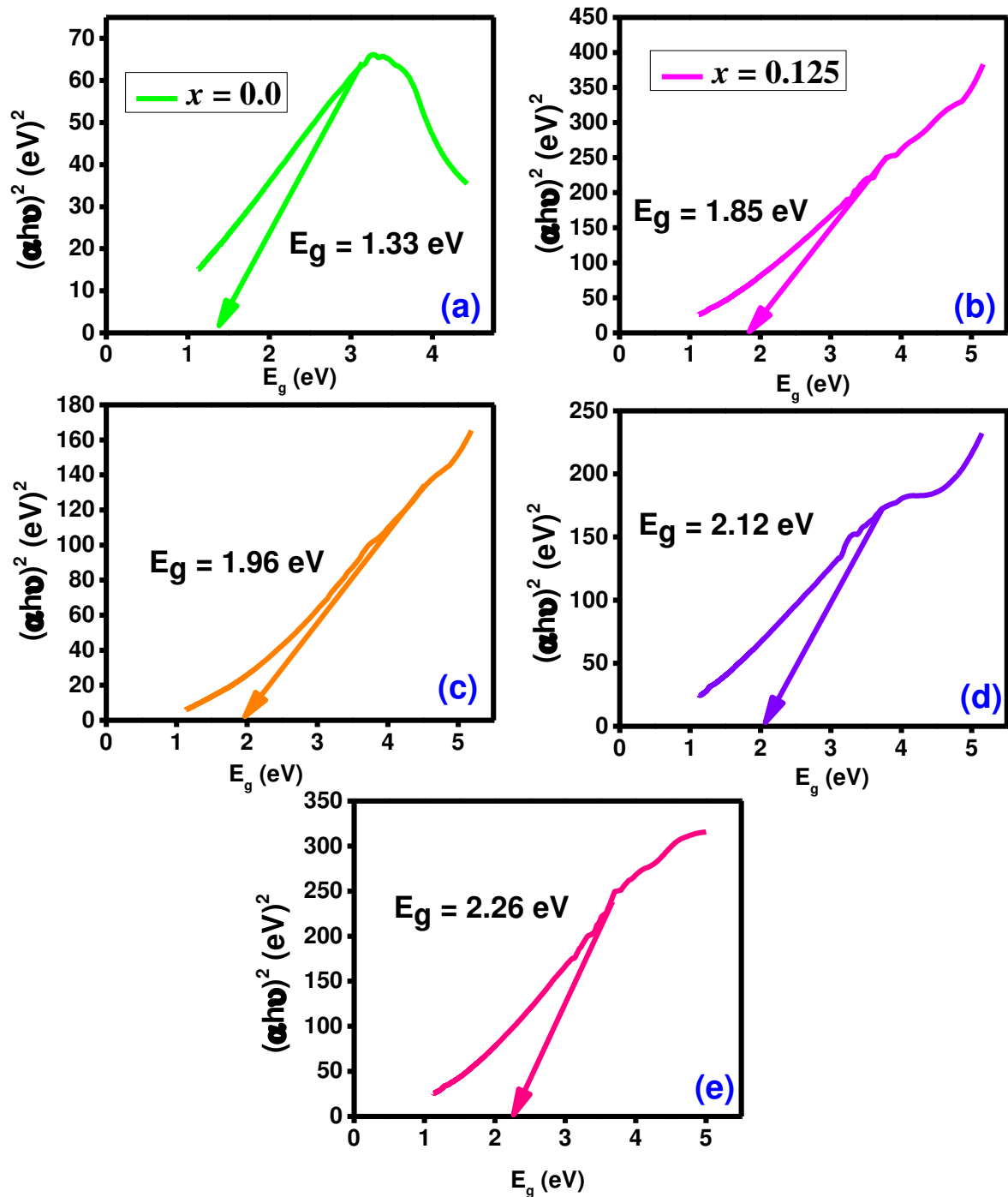


Fig. 7 Tauc's plots for Ni-CCMCF samples

3.5 Electrical resistivity of Ni-CCMCF samples

Electrical dc resistivity is a property of a substance that prevents electrons from flowing through it. The electrical properties of the spinel matrix were altered by the partial replacement of Fe^{3+} with divalent and trivalent cations, which caused lattice distortion and strain. The electrical resistivity (ρ) depends on the doping ion and preparation process of the ferrite [7]. The electrical resistivity was found through equation (16) [27]:

$$\rho = RA/L \quad (16)$$

The log of resistivity with the inverse of temperature plots is depicted in Fig. 8. It is clear from Fig. 8 that the resistivity curves break into two regions due to the phase transition from ferromagnetic to paramagnetic state and the point where a break (kink) occurs called Curie temperature (T_c). It was noted from Fig. 9(a-b) that the resistivity was maximum for Ni^{2+} concentration $x = 0.375$ in the Ferro region and for Ni^{2+} concentration $x = 0.125$ in the para region. The process known as Verwey's hopping can explain this electrical resistivity behaviour. In spinel ferrites, conduction takes place through an electron hopping mechanism exchange of Fe^{3+} (ferric) \leftrightarrow Fe^{2+} (ferrous) ions occur on an octahedral site. The distance between ions as well as the activation energy has a significant impact on the hopping process. When compared to the distance between two metal ions on the tetrahedral and octahedral sites, the two metal ions at B-site are substantially closer to each other. As a result, hopping between two metal ions on the same site is significantly easier than hopping between two distinct sites. As a result, there is no hopping between the A- and B- sites since ferric ions exclusively exist at B-site and ferrous ions have accommodation on the B-site [38].

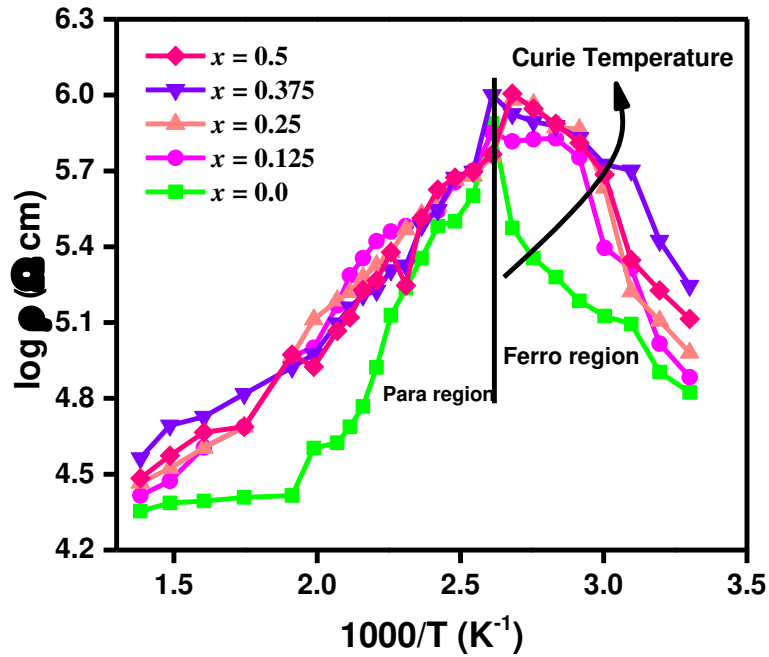


Fig. 8 $1000/T$ versus $\log \rho$ for Ni-CCMCF samples

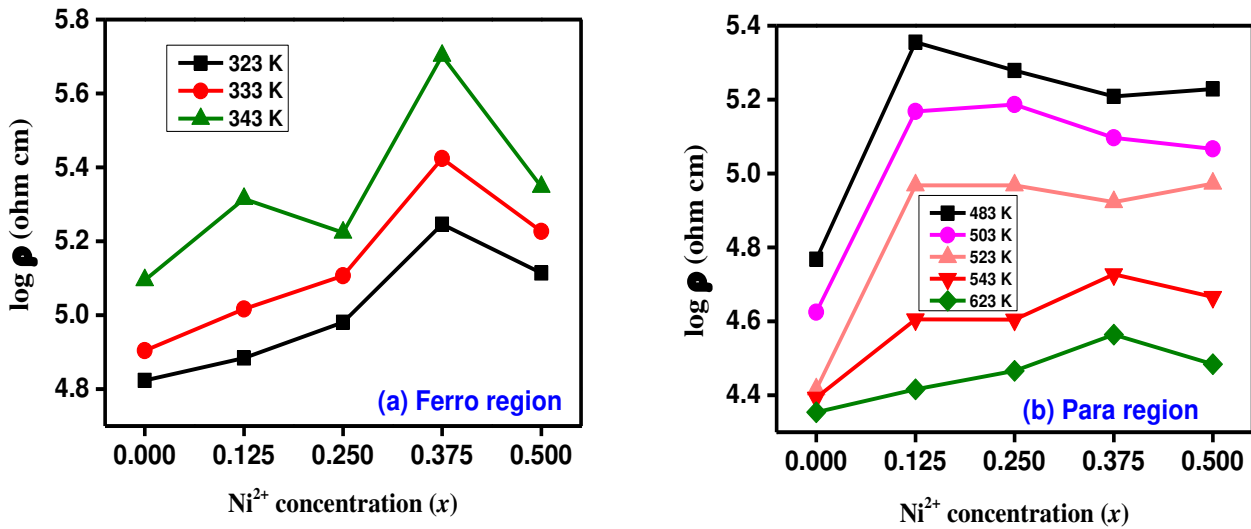


Fig. 9(a-b) Ni^{2+} concentration (x) versus the log of resistivity in Ferro and para region at different temperatures

3.6 Dielectric analysis of Ni-CCMCF samples

Fig. 10(a) showed the dielectric constant fluctuation with frequency for Ni-CCMCF samples. It was seen that the dielectric constant reduces with raising frequency. According to Koop's phenomenological theory, this dispersion in dielectric behaviour is caused by Maxwell-Wagner-type interfacial polarization [39]. At lower frequencies, the high dielectric constant is ascribed to the inhomogeneous dielectric structure caused by space charge polarization [40].

Electrical polarization in ferrites is caused by the directed electric field created by electron exchange between Fe^{2+} and Fe^{3+} ions. When the frequency is increased, the electronic exchange cannot follow the alternating field, after a drop in the dielectric constant was observed. The number of electrons exchanged is determined in the *B*- site by the concentration of $\text{Fe}^{3+}/\text{Fe}^{2+}$ ions. The dielectric tangent loss ($\tan \delta_e$) is a significant component of total core loss in ferrites [41]. The structural homogeneity, the quantity of Fe^{2+} ions, and synthesis variables including sintering time, temperature, and heat all influence the magnitude of the loss tangent. The fluctuation of “ $\log f$ ” as a function of “ $\tan \delta_e$ ” is shown in Fig. 10(b). Because charge hopping between Fe^{2+} and Fe^{3+} can only follow the frequency of the field up to a certain point, the “ $\tan \delta_e$ ” drops as the frequency increases. The potential uses of spinel ferrites in high-frequency microwave devices are demonstrated by the low dielectric tangent loss values at higher frequencies [42]. For the manufacturing of high-frequency devices, a material with a low value of dielectric tangent losses is used [43].

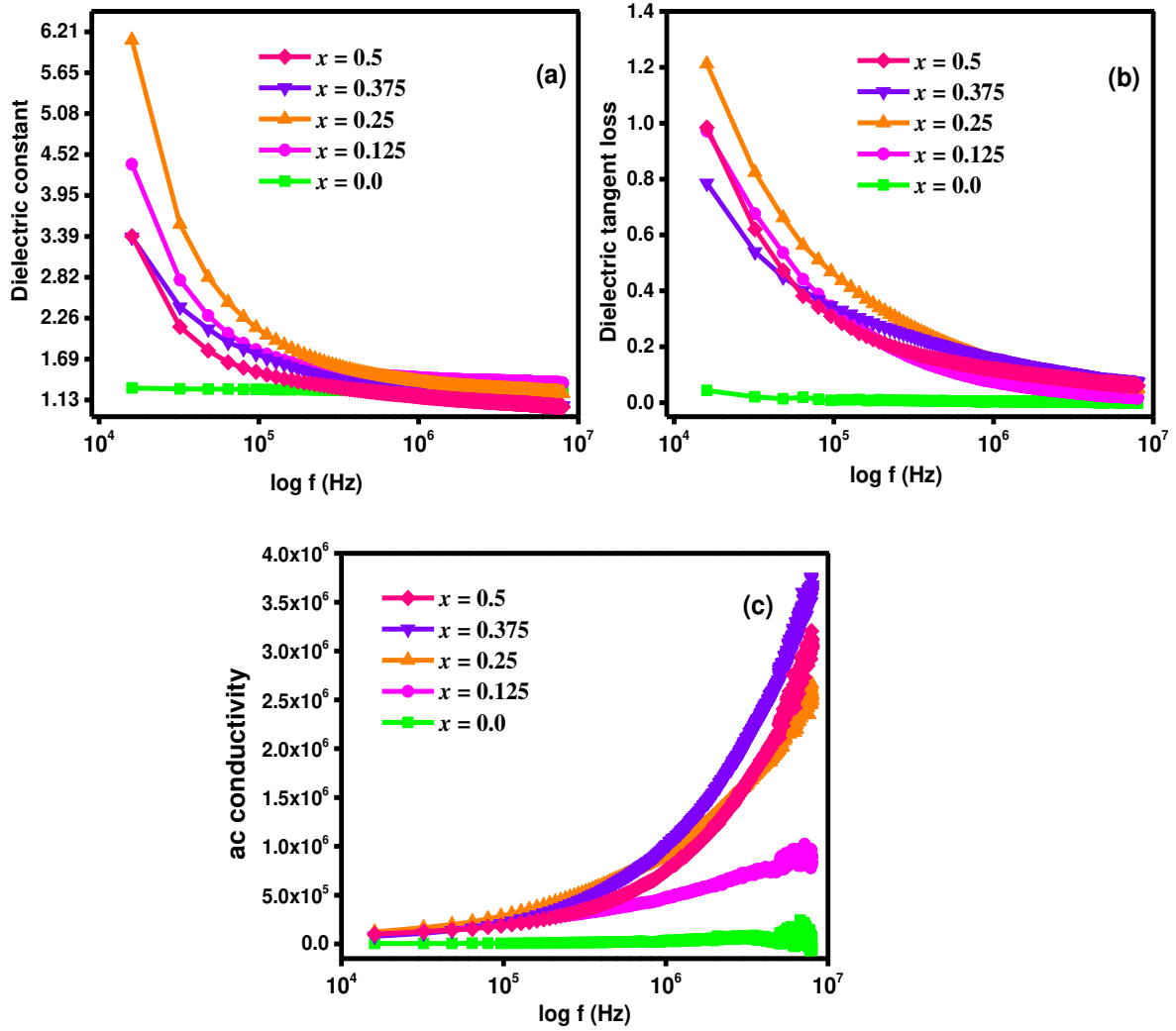


Fig. 10 log of frequency *versus* (a) dielectric constant (b) tangent loss (c) *ac* conductivity of Ni-CCMCF samples

The *ac* conductivity (σ_{ac}) of the Ni-CCMCF samples was estimated by using relation ($\sigma_{ac} = 2\pi f \tan \delta$) to better understand the conduction process. The variation of the log of frequency *versus* *ac* conductivity (σ_{ac}) is depicted in Fig. 10(c). Fig. 10(c) revealed that “ σ_{ac} ” increases as frequency increases. The value of “ σ_{ac} ” was found to be constant at low frequency and dramatically rises in the high-frequency region. The mechanism of electrical conduction is generally known to be the same as that of dielectric polarization. As the frequency rises, the “ σ_{ac} ” steadily increases. Because grain boundaries are more efficient than grains in electrical conduction at lower frequencies, Fe²⁺, and Fe³⁺ ion hopping is confined at lower frequencies. The conductive grains become more active and promote the conduction process as the frequency of the applied field rises [41].

In the real part of impedance (Z') *versus* the imaginary part of impedance (Z'') plots as shown in Fig.11, each RC component of the equivalent circuit produces a semicircle (Cole-

Cole diagram). A single semicircle at a higher frequency in a Z' versus Z'' plots indicate the presence of grain effect, a second semicircle at a lower frequency indicates the presence of grain boundary effect. The grain boundary impedance is caused by the random alignment of grains [44].

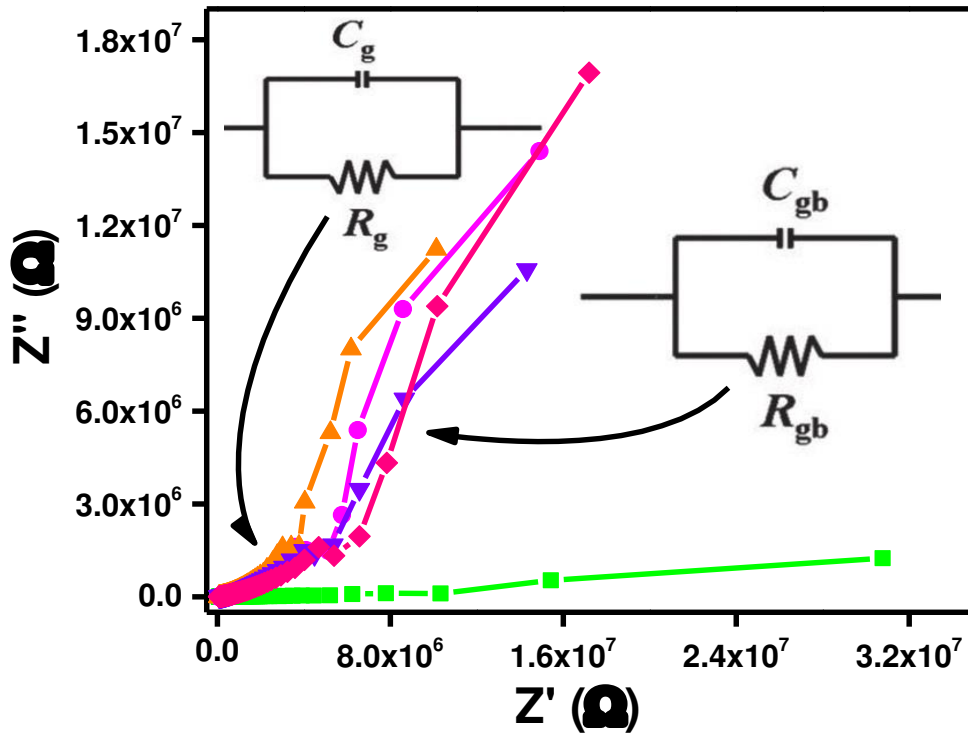


Fig. 11 Cole-Cole plots for Ni-CCMCF samples

The plots of the log of frequency versus magnetic tangent loss ($\tan \delta_m$) is depicted in Fig. 12(a). It was observed from Fig. 12(a) that the values of “an δ_m ” was reduced with increasing frequency and showed a higher value at low frequency. It is found that when frequency increases, the magnetic loss factor decreases. Due to imperfections in the lattice, there is a loss caused by the lag in the motion of the domain walls in response to the applied alternating field [45]. The real part of initial permeability (μ') is determined via relation [46]: $\mu' = \frac{L_S}{L_o}$, where L_S and L_o are the inductance of solenoid coil with and without the sample, respectively and $L_o = \frac{\mu_o N^2 A}{l}$ where $\mu_o = 4\pi \times 10^{-7}$ H/m is permeability of free space, N is the number of turns of the solenoid, A is the area of the pellet, and l is the length of the solenoid. The plots of the log of frequency versus real (μ') and imaginary ($\mu'' = \mu' \times \tan \delta_m$) part of initial permeability are given in the Fig. 12(b) and Fig. 12(c), respectively. The curves in Fig. 12(b) have the property that, for the samples except $x = 0.5$, μ' is constant up to a critical frequency and then rapidly decreases. For permeability values over a certain point, the

resonance occurs at a lower frequency. The matching of the magnetic dipole's oscillation frequency with the applied frequency causes energy to be absorbed, which leads to the resonance frequency peaks. The appearance of the imaginary part of initial permeability (μ'') is caused by the domain walls' mobility lagging behind the applied alternating field. This conduct reflects a typical character involved in relaxation. It may be because of the domain walls' irreversible displacement [47].

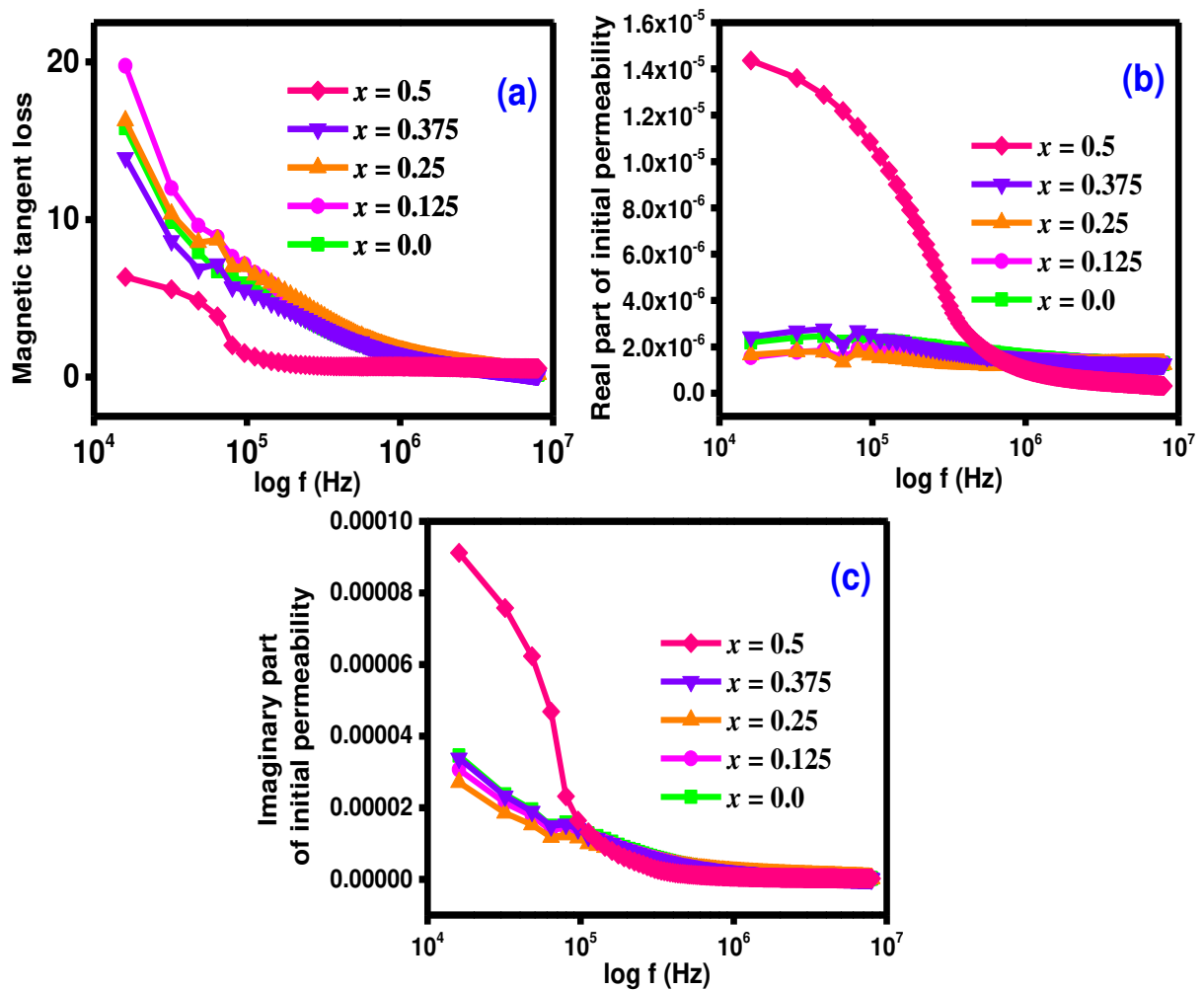


Fig. 12 log of frequency *versus* (a) magnetic tangent loss (b) real part of initial permeability (c) imaginary part of initial permeability of Ni-CCMCF samples

3.7 Magnetic analysis of Ni-CCMCF samples

Hysteresis ($M-H$) loops for Ni-CCMCF samples are depicted in Fig. 13(a). A magnetic energy loss can be seen in the region of the $M-H$ loops. This region is small for each sample, which revealed the soft ferrite nature of Ni-CCMCF samples. The values of different magnetic parameters are given in Table 4. The saturation magnetization (M_s) was decreased when magnetic Ni^{2+} ions ($2\mu_B$) replace by nonmagnetic Mg^{2+} ($0\mu_B$) ions [48]. Smaller crystallites have lower saturation magnetization, which may be explained by surface distortions produced

by the interaction of transition metal ions with the oxygen atoms in the spinel lattice. The net magnetic moment decreases as a result. Because of the large surface-to-volume ratio, the disorder and frustration at the surface grow with size reduction, reducing the magnetic interaction between bonds [49]. The studied sample's coercivity (H_c) varies from 370.43 to 586.38 Oe. Large magneto-crystalline anisotropy of Ni^{2+} is thought to be the cause of the increase in coercive values. Material intrinsic properties such as magneto-crystalline anisotropy play a significant effect on coercivity [49]. The measured squareness ratio ($SQ = M_r/M_s$) for Ni^{2+} doped CCMCF samples is less than 0.5. This indicates that magneto static interactions for the particle's interaction. Additionally, the low value of the SQ represents the presence of cubic anisotropic single-domain particles in the Ni-CCNCF samples. The anisotropy constant ($K = H_c \times M_s / 0.96$) and initial permeability ($\mu_i = M_s^2 \times D / K$) were determined as enlisted in Table 4. The value of the anisotropy constant and initial permeability was decreased with the addition of Ni^{2+} cations. The microwave frequency was measured to study the behaviour of as-prepared samples in a microwave application. The relation $\omega_m = 8\pi^2 M_s \gamma$ was applied to calculate the high-frequency (where $\gamma = 2.8$ MHz/Oe is the gyromagnetic ratio) [50, 51]. Fig. 13(b) indicated that the microwave frequency response of Ni-CCMCF ferrites is a favorite candidate for high-frequency devices. However, the as-prepared magnetic materials were found to be operated in the microwave frequency range of 8.88 – 17.43 GHz.

Table 4 Magnetic parameters for Ni-CCMCF samples

x	H_c (Oe)	SQ	M_r (emu/g)	M_s (emu/g)	K (erg/cm ³)	μ_i	ω_m (GHz)
0.0	370.43	0.403	31.79	78.86	30429.28	11.71	17.43
0.125	573.32	0.438	33.34	76.03	45405.74	6.11	16.81
0.25	507.18	0.399	20.9	52.34	27651.87	4.44	11.57
0.375	502.79	0.376	17.11	45.41	23783.01	2.87	10.04
0.5	586.38	0.357	14.38	40.18	24542.44	0.69	8.88

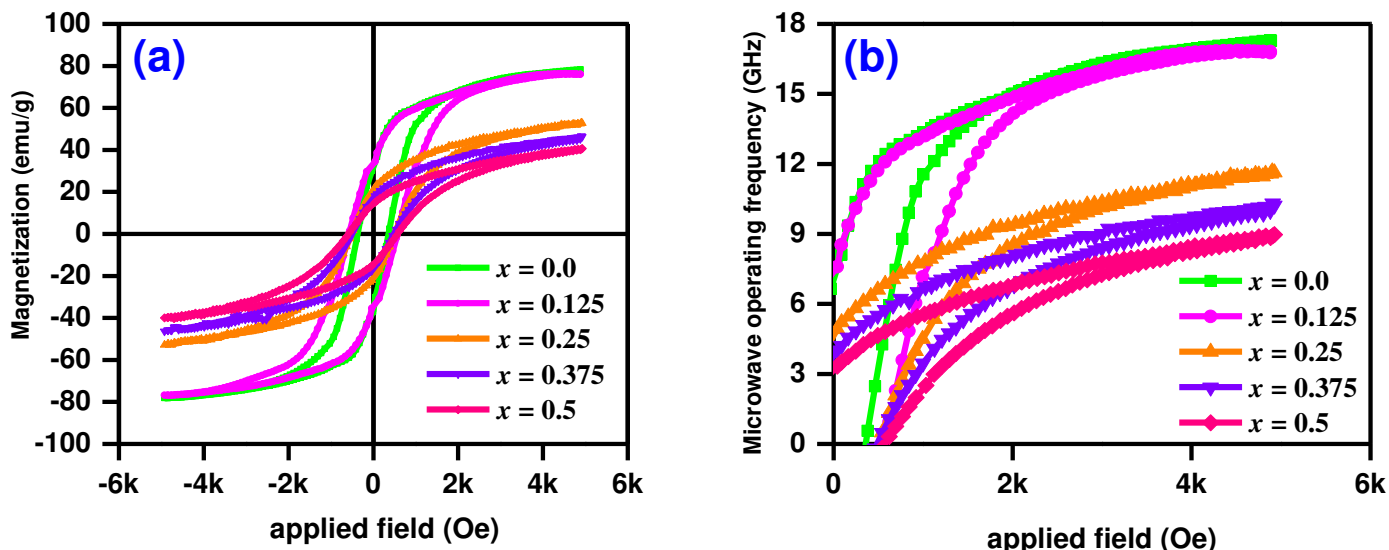


Fig. 13(a) *M-H* loops for Ni-CCMCF samples **(b)** applied field *versus* microwave operating frequency for Ni-CCMCF samples

3.8 Morphological and compositional analysis of Ni-CCMCF sample $x = 0.025$

The micrograph for the Ni-CCMCF ($x = 0.025$) sample is depicted in Fig. 14(a) and agglomeration is observed in Ni-CCMCF ($x = 0.025$) sample powder. This has been attributed to magnetic dipole interactions between ferrite particles [52]. EDS analysis (Fig. 14(b)) was revealed the presence and composition of all elements present in the samples, which also in agreement with XPS analysis.

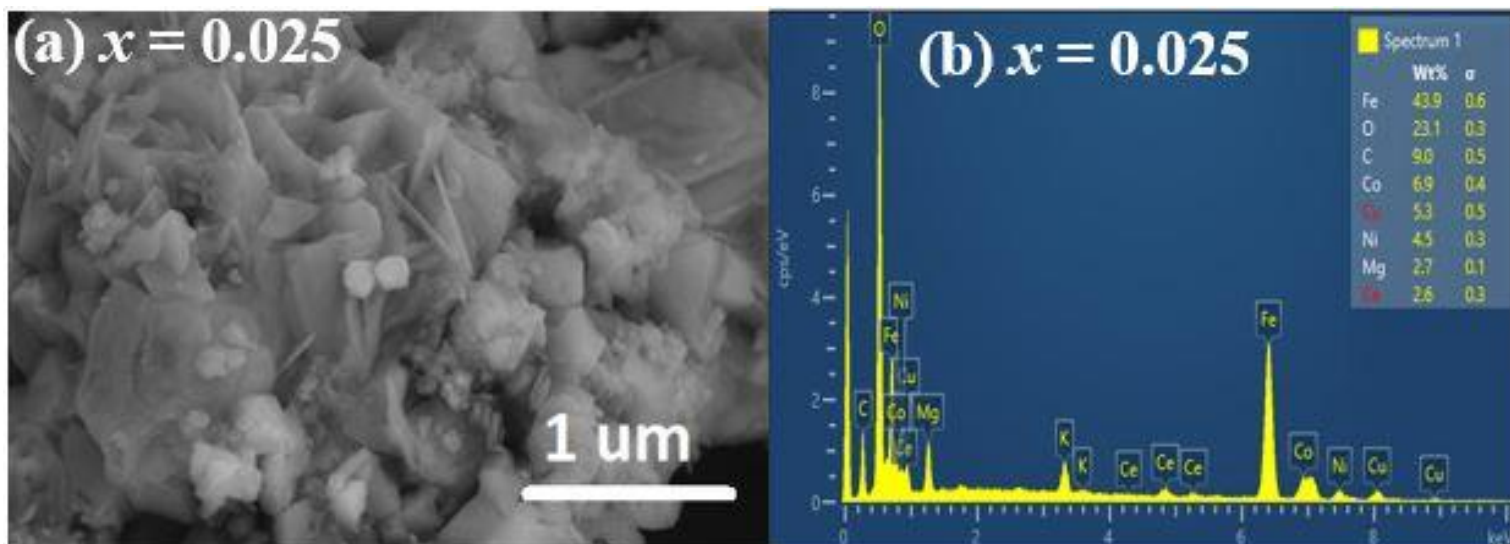


Fig. 14(a) FE-SEM micrograph for sample $x = 0.025$ **(b)** EDS spectrum for sample $x = 0.025$

3.9 XPS analysis of Ni-CCMCF sample $x = 0.025$

Binding energy values were recorded using an XPS analysis to identify the elements and their valence states, as well as the effect of cation distribution among spinel A- and B- sites. The XPS spectra of the Ni-CCMCF ($x = 0.025$) sample are demonstrated in Fig. 15 and Fig.

16. The survey scan (Fig. 15) was collected to identify the elements that exist on the surface of the sample. The observed elements are carbon, oxygen, nickel, cobalt, copper, cerium, and iron only as we were expecting which was also confirmed by EDS analysis (as seen in Fig. 14(b)). The high-resolution spectra of C1s, O1s, Ni2p, Co2p, Cu2p, Ce3d, and Fe2p core level spectra were collected for comprehensive analysis shown (supporting information confirms the presence of all other elements). The detailed scan of F2p shown in Fig. 16 has two noticeable peaks at 710.5 eV and 724.05 eV which corresponds to Fe2p_{3/2} and Fe2p_{1/2} spin-orbit splitting, respectively [53]. Meanwhile broader peak appeared around 718.3 eV and is associated with the satellite peak of Fe [54]. The first peak Fe2p_{3/2} is resolved into two sub-peaks leveled at 710.45 eV and 712.38 eV which are assigned to Fe²⁺(ferrous) and Fe³⁺ (ferric). These results are consistent with already reported studies [54-56]. The co-existence of Fe³⁺ and Fe²⁺ facilitates the hopping mechanism exchange process.

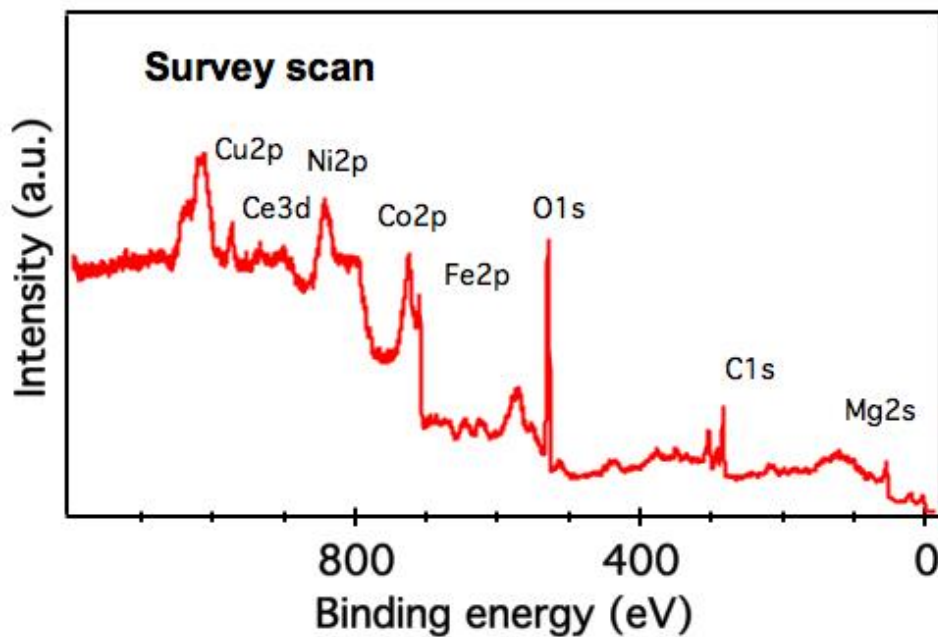


Fig. 15 XPS survey scan for sample $x = 0.025$

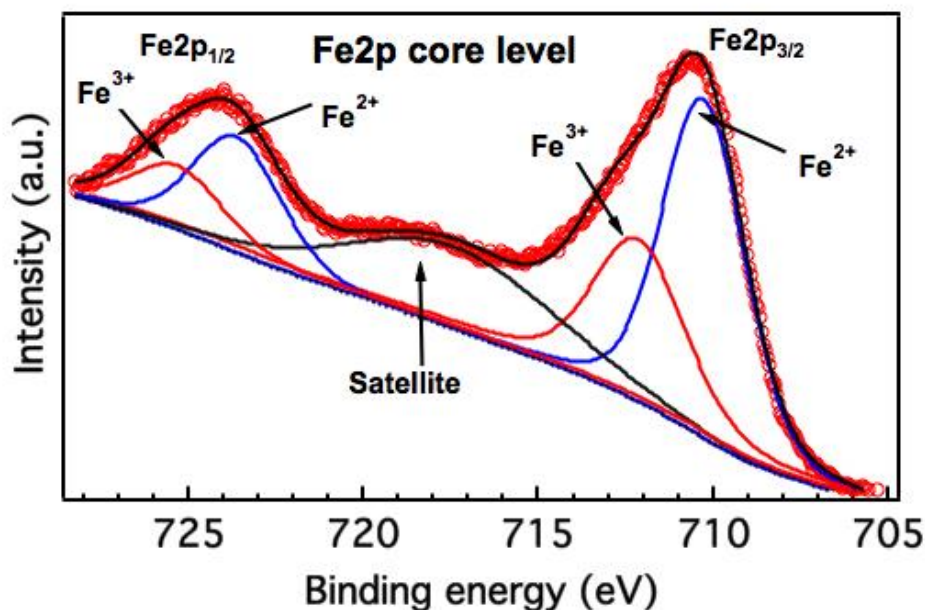


Fig. 16 XPS high-resolution spectrum of Fe2p core level

4 Conclusions

The Ni-CCMCF spinel ferrites were prepared by the SGAC method. The high crystallinity was observed in XRD spectra and from 8.3694 Å to 8.3410 Å the lattice constant was reduced. The crystallite size was also reduced from 57.33 ± 0.05 to 10.15 ± 0.05 nm with the doping of Ni^{2+} ions. Moreover, the specific surface area was enhanced due to the replacement of Ni^{2+} ions. The absorption bands and Raman modes also confirmed the replacement of Ni^{2+} ions in the spinel matrix. The minimum optical bandgap was 0.87 eV for Ni^{2+} doping $x = 0.0$ and the maximum 1.68 eV for Ni^{2+} doping $x = 0.5$. The resistivity was observed with minimum Ferro and para regions for the pure CCMCF sample. The tangent loss and dielectric constant were reduced with increasing frequency. EDS and XPS analysis revealed the presence of all the compositional elements. For the pure CCMCF sample, the minimum tangent loss was found. Hence, due to the smaller tangent loss, the as-prepared CCMCF sample will be used for high resonant frequency applications.

References

- [1] K. Hussain, N. Amin, M.I. Arshad, *Ceramics International*, 47 (2021) 3401-3410.
- [2] A. Rana, V. Kumar, *ECS Journal of Solid State Science and Technology*, 10 (2021) 031005.
- [3] H. Jalili, B. Aslibeiki, N. Eskandarzadeh, *Iranian Journal of Physics Research*, 21 (2021) 219-242.
- [4] T. Zhou, S. Cao, N. Sui, J. Tu, T. Zhang, *Sensors and Actuators B: Chemical*, (2021) 130152.
- [5] P. Kumar, S. Pathak, A. Singh, H. Khanduri, X. Wang, G. Basheed, R.P. Pant, *Materials Chemistry and Physics*, 265 (2021) 124476.
- [6] S. Woltz, R. Hiergeist, P. Görnert, C. Rüssel, *Journal of magnetism and magnetic materials*, 298 (2006) 7-13.

- [7] A.U. Rehman, N. Morley, N. Amin, M.I. Arshad, M.A. un Nabi, K. Mahmood, A. Ali, A. Aslam, A. Bibi, M.Z. Iqbal, *Ceramics International*, 46 (2020) 29297-29308.
- [8] G. Abbas, A.U. Rehman, W. Gull, M. Afzaal, N. Amin, L. Ben Farhat, M. Amami, N.A. Morley, M. Akhtar, M.I. Arshad, *Journal of Sol-Gel Science and Technology*, 101 (2022) 428-442.
- [9] G. Hussain, I. Ahmed, A.U. Rehman, M.U. Subhani, N. Morley, M. Akhtar, M.I. Arshad, H. Anwar, *Journal of Alloys and Compounds*, (2022) 165743.
- [10] I. ALIa, N. Amin, A. REHMAN, M. Akhtar, M. Fatima, K. Mahmood, A. ALIa, G. Mustafa, M. Hasan, A. Bibi, *Digest Journal of Nanomaterials Biostructures*, 15 (2020), 67-73.
- [11] A. Aslam, A.U. Rehman, N. Amin, M.A. un Nabi, Q. ul ain Abdullah, N. Morley, M.I. Arshad, H.T. Ali, M. Yusuf, Z. Latif, *Journal of Physics and Chemistry of Solids*, 154 (2021) 110080.
- [12] N. Amin, M. Akhtar, M. Sabir, K. Mahmood, A. ALIa, G. Mustafa, M. Hasan, A. Bibi, M. Iqbal, F. Iqbal, *Journal of Ovonic Research*, 16 (2020) 11-19.
- [13] A. Aslam, A. Razzaq, S. Naz, N. Amin, M.I. Arshad, M. Nabi, A. Nawaz, K. Mahmood, A. Bibi, F. Iqbal, *Journal of Superconductivity and Novel Magnetism*, 34 (2021) 1855-1864.
- [14] M.I. Arshad, M. Hasan, A.U. Rehman, M. Akhtar, N. Amin, K. Mahmood, A. Ali, T. Trakoolwilaiwan, N.T.K. Thanh, *Ceramics International*, 48 (2022) 14246-14260.
- [15] S.Y. Mulushoa, N. Murali, M.T. Wegayehu, S. Margarete, K. Samatha, *Results in physics*, 8 (2018) 772-779.
- [16] J. Domínguez-Arvizu, J. Jiménez-Miramontes, J. Salinas-Gutiérrez, M. Meléndez-Zaragoza, A. López-Ortiz, V. Collins-Martínez, *International journal of hydrogen energy*, 42 (2017) 30242-30248.
- [17] T. Peng, X. Zhang, H. Lv, L. Zan, *Catalysis communications*, 28 (2012) 116-119.
- [18] K. Dileep, B. Loukya, N. Pachauri, A. Gupta, R. Datta, *J. Appl. Phys.*, 116 (2014) 103505.
- [19] R.S. Gaikwad, S.-Y. Chae, R.S. Mane, S.-H. Han, O.-S. Joo, *International Journal of Electrochemistry*, 2011 (2011).
- [20] N.S. Kumar, N. Das, K. Devlal, S. Seema, M. Shekhawat, M. Hidayath, S.A. Khader, *AIP Conf. Proc.*, AIP Publishing LLC, 2020, pp. 110043.
- [21] L. Yu, A. Sun, N. Suo, Z. Zuo, X. Zhao, W. Zhang, L. Shao, Y. Zhang, *Journal of Materials Science: Materials in Electronics*, 31 (2020) 14961-14976.
- [22] X. Pan, A. Sun, Y. Han, W. Zhang, X. Zhao, J. Zou, *Phys. Status Solidi*, 256 (2019) 1800511.
- [23] D. Varshney, K. Verma, *Materials Chemistry and Physics*, 140 (2013) 412-418.
- [24] R. Ali, A. Mahmood, M.A. Khan, A.H. Chughtai, M. Shahid, I. Shakir, M.F. Warsi, *Journal of Alloys and Compounds*, 584 (2014) 363-368.
- [25] A. Aslam, A. Razzaq, S. Naz, N. Amin, M.I. Arshad, M.A.U. Nabi, A. Nawaz, K. Mahmood, A. Bibi, F. Iqbal, *Journal of Superconductivity and Novel Magnetism*, (2021) 1-10.
- [26] A. Aslam, A.U. Rehman, N. Amin, M. Amami, M. Nabi, H. Alrobei, M. Asghar, N. Morley, M. Akhtar, M.I. Arshad, *Journal of Superconductivity and Novel Magnetism*, (2021) 1-11.
- [27] N. Amin, A. Razaq, A.U. Rehman, K. Hussain, M. Nabi, N. Morley, M. Amami, A. Bibi, M.I. Arshad, K. Mahmood, *Journal of Superconductivity and Novel Magnetism*, (2021) 1-11.
- [28] M.I.U. Haq, M. Asghar, M.A.U. Nabi, N. Amin, S. Tahir, M.I. Arshad, *Journal of Superconductivity and Novel Magnetism*, 35 (2022) 719-732.
- [29] R. Zakir, S.S. Iqbal, A.U. Rehman, S. Nosheen, T.S. Ahmad, N. Ehsan, F. Inam, *Ceramics International*, 47 (2021) 28575-28583.
- [30] K. Hussain, A. Bibi, F. Jabeen, N. Amin, K. Mahmood, A. Ali, M.Z. Iqbal, M. Arshad, *Physica B: Condensed Matter*, 584 (2020) 412078.

- [31] X. Huang, A. Sun, Y. Jiang, J. Wang, Y. Zhang, L. Shao, *Applied Physics A*, 127 (2021) 1-11.
- [32] N.B. Velhal, N.D. Patil, A.R. Shelke, N.G. Deshpande, V.R. Puri, *AIP Advances*, 5 (2015) 097166.
- [33] A. Aslam, N. Morley, N. Amin, M.I. Arshad, M.A. un Nabi, A. Ali, K. Mahmood, A. Bibi, F. Iqbal, S. Hussain, *Physica B: Condensed Matter*, 602 (2021) 412565.
- [34] A. Elahi, M. Ahmad, I. Ali, M. Rana, *Ceramics International*, 39 (2013) 983-990.
- [35] A.U. Rehman, N. Amin, M.B. Tahir, M.A. un Nabi, N. Morley, M. Alzaid, M. Amami, M. Akhtar, M.I. Arshad, *Materials Chemistry and Physics*, (2021) 125301.
- [36] A. Aslam, A.U. Rehman, N. Amin, M. Amman, M. Akhtar, N. Morley, M.S. Al-Sharif, M. Hessien, K.A. El-Nagdy, M.I. Arshad, *Materials Chemistry and Physics*, (2022) 127034.
- [37] N. Barde, V. Rathod, P. Solanki, N. Shah, P. Bardapurkar, *Applied Surface Science Advances*, 11 (2022) 100302.
- [38] G. Aravind, D. Ravinder, V. Nathaniel, *Physics research international*, 2014 (2014), 672739.
- [39] R. Kharabe, R. Devan, C. Kanamadi, B. Chougule, *Smart Materials and Structures*, 15 (2006) N36.
- [40] M. Shelar, P. Jadhav, S. Chougule, M. Mallapur, B. Chougule, *Journal of Alloys and Compounds*, 476 (2009) 760-764.
- [41] M. Dar, D. Varshney, *Journal of Magnetism and Magnetic Materials*, 436 (2017) 101-112.
- [42] M. Raghasudha, D. Ravinder, P. Veerasomaiah, *Materials Sciences and Applications*, 4 (2013) 33805.
- [43] M. Junaid, I. Kousar, S. Gulbadan, M.A. Khan, M.A. Yousuf, M.M. Baig, G.A. Ashraf, H. Somaily, M. Morsi, *Physica B: Condensed Matter*, 641 (2022) 414120.
- [44] S. Haque, S.C. Mazumdar, M.N.I. Khan, M.K. Das, *Materials Sciences and Applications*, 12 (2021) 121-138.
- [45] U. Gawas, V. Verenkar, V. Vader, A. Jain, S.S. Meena, *Materials Chemistry and Physics*, 275 (2022) 125250.
- [46] M. El Nimr, B. Moharram, S. Saafan, S. Assar, *Journal of magnetism and magnetic materials*, 322 (2010) 2108-2112.
- [47] S.M. Hoque, M.S. Ullah, F. Khan, M. Hakim, D. Saha, *Physica B: Condensed Matter*, 406 (2011) 1799-1804.
- [48] E.E. Ateia, A.A. El-Bassuony, G. Abdellatif, A.T. Mohamed, *Silicon*, 10 (2018) 1687-1696.
- [49] R. Sharma, P. Thakur, P. Sharma, V. Sharma, *Journal of Alloys and Compounds*, 704 (2017) 7-17.
- [50] A. Majeed, M.A. Khan, F. ur Raheem, A. Hussain, F. Iqbal, G. Murtaza, M.N. Akhtar, I. Shakir, M.F. Warsi, *Journal of magnetism and magnetic materials*, 408 (2016) 147-151.
- [51] S. Gaba, A. Kumar, P.S. Rana, M. Arora, *Journal of Magnetism and Magnetic Materials*, 460 (2018) 69-77.
- [52] M.P. Dojcinovic, Z.Z. Vasiljevic, V.P. Pavlovic, D. Barisic, D. Pajic, N.B. Tadic, M.V. Nikolic, *Journal of Alloys and Compounds*, 855 (2021) 157429.
- [53] P.S. Bagus, C.J. Nelin, C.R. Brundle, N. Lahiri, E.S. Ilton, K.M. Rosso, *The Journal of Chemical Physics*, 152 (2020) 014704.
- [54] L. Li, P. Ma, S. Hussain, L. Jia, D. Lin, X. Yin, Y. Lin, Z. Cheng, L. Wang, *Sustainable Energy and Fuels*, 3 (2019) 1749-1756.
- [55] A.L. Smeigh, J.E. Katz, B.S. Brunschwig, N.S. Lewis, J.K. McCusker, *The Journal of Physical Chemistry C*, 112 (2008) 12065-12068.
- [56] B. Lynch, F. Wiame, V. Maurice, P. Marcus, *Applied Surface Science*, 575 (2022) 151681.